Ceramics International 50 (2024) 35421–35429

Contents lists available at ScienceDirect

Ceramics International

journal homepage: www.elsevier.com/locate/ceramint

Enhancing cutting tool durability: Exploration of Al_2O_3-SiC_w-graphene composites fabricated by SPS for improved mechanical and scratch resistance

Marta Suárez [a,*], Rut Benavente [b], Amparo Borrell [b,**], Ana M. Pérez-Mas [c,d], Rosa Menéndez [c], Carlos F. Gutiérrez [e], Adolfo Fernández [a]

[a] Centro de Investigación en Nanomateriales y Nanotecnología (CINN-CSIC), Universidad de Oviedo (UO), Principado de Asturias (PA), Avda. de la Vega, 4-6, 33940, El Entrego, Spain
[b] Instituto Universitario de Investigación en Tecnología de Materiales (IUITM), Universitat Politècnica de València, Camino de Vera, S/n, 46022, Valencia, Spain
[c] Instituto de Ciencia y Tecnología del Carbono (INCAR), CSIC, Fe 26, Francisco Pintado, Oviedo, 33011, Spain
[d] Departamento de Física, Universidad de Oviedo, 33204, Spain
[e] Nanoker Research S.L. Polígono Industrial de Olloniego, parcela 22[a], Nave 5, Oviedo, Asturias, 33660, Spain

ARTICLE INFO

Handling Editor: Dr P. Vincenzini

Keywords:
D. graphene-ceramic
A. Spark plasma sintering
C. Scratch resistance
E. Cutting tools

ABSTRACT

This study focuses on the fabrication and characterisation of Al_2O_3-SiC_w-rGO composites sintered by spark plasma sintering (SPS) technique. The research is mainly focused on understanding the impact of varying graphene content (0.5, 1.0 and 1.5 vol %) on nanomechanical properties and scratch resistance. Among the compositions investigated, the composite containing 0.5 vol% graphene showed superior mechanical properties. Specifically, it exhibited a hardness of ~30 GPa, a fracture toughness of 10.5 MPa $m^{1/2}$ and a flexural strength of ~920 MPa. In addition, this composite showed remarkable scratch resistance compared to composites with a higher or lower graphene content. In addition to mechanical properties, the fabricated composites also exhibited high electrical conductivity. This characteristic is especially advantageous for electrical discharge machining (EDM) processes. The high electrical conductivity enables efficient machining of complex shapes by EDM, thereby reducing machining costs while ensuring accuracy and efficiency.

1. Introduction

Cutting tools play an integral role in our daily lives, facilitating various machining operations. The effectiveness of these tools relies heavily on the choice of materials used for their construction, which must be suitable for the specific machining processes, workpiece materials, and thermomechanical conditions available. Historically, carbon tool steels dominated the cutting tool landscape before the 20th century [1]. However, the advent of high-speed steel (HSS) revolutionised the industry by enabling a fourfold increase in cutting speed, owing to the inclusion of alloying elements that form robust carbides [2]. In the early 20th century, an alloy of cobalt and chromium, which was non-magnetic and resistant to wear and corrosion, emerged briefly before being surpassed by cutting tools crafted from carbides (such as WC, TiC, TaC, NbC) and ceramic materials (both oxidic and non-oxidic ceramics) [1]. Presently, ceramic composites are at the forefront of advanced cutting tool fabrication, particularly in extreme operating conditions such as dry machining processes [3]. The demand for these components is substantial, and advancements in the development of longer-lasting materials promise significant economic benefits.

Several material properties are critical in this application, including hardness, Young's modulus, fracture toughness, wear resistance, and scratch resistance. Alumina, due to its exceptional hardness, is a commonly used ceramic material in cutting tool production [4]. However, its brittle nature and low flexural strength and toughness necessitate the incorporation of a reinforcing second phase. Silicon carbide has emerged as an ideal candidate, boasting extraordinary hardness and high-temperature strength [5]. The Al_2O_3–SiC ceramic composite exhibits enhanced fracture resistance, marking a substantial improvement in the reliability and abrasive wear resistance of ceramic cutting tools

* Corresponding author.
** Corresponding author.
E-mail addresses: m.suarez@cinn.es (M. Suárez), aborrell@upv.es (A. Borrell).

https://doi.org/10.1016/j.ceramint.2024.06.353
Received 7 May 2024; Received in revised form 18 June 2024; Accepted 25 June 2024
Available online 26 June 2024

[6].

However, machining these materials proves challenging with traditional techniques, often requiring expensive diamond tools. To overcome this obstacle, introducing an electrically conductive phase such as TiC, WC, TiN, or graphene can render the composite amenable to machining through alternative methods such as electrical discharge machining (EDM), ultrasonic machining, or laser machining, promising cost-effective processing times for finishing cutting tools [7–9].

Graphene, one of the most ground-breaking materials of recent years, boasts an unprecedented combination of mechanical, electrical, and thermal properties, positioning it as a promising candidate across various application fields [10–12]. Beyond its standalone properties, incorporating graphene as a functional additive in advanced composite materials holds substantial potential for materials science and technology development. While initial research focused on polymer matrices [13,14], there is growing interest in integrating graphene into metallic and ceramic matrices [15–17].

In the field of ceramics, incorporating graphene offers two primary benefits. Firstly, even low graphene contents can impart electrical conductivity to ceramics [18]. Secondly, graphene layers serve as effective reinforcements against brittleness, which is a significant limitation of ceramic materials [19,20]. Nevertheless, the preparation of carbon-ceramic composites presents its own set of challenges. Graphene's poor wettability with ceramics can be mitigated by using graphene oxide (GO) as the starting material, as the polar functional groups on GO's edges facilitate intimate mixing with ceramic powders [21]. Additionally, the presence of carbon components within ceramic matrices complicates the densification process, which can be addressed by employing non-conventional sintering techniques such as spark plasma sintering (SPS), already successfully employed with ceramic-carbon nanotube and ceramic-carbon nanofibre composites [22,23].

Notably, intriguing synergistic effects arise when graphene is incorporated into ceramics and sintered using SPS. This includes the homogenous flow of electrical current through the materials during heating and the in-situ reduction of graphene oxide to graphene under specific sintering conditions (high temperature, vacuum environment, and inside a graphite mould) [21]. With these premises in mind, this study aims to explore the successful fabrication of Al_2O_3-SiC_w-rGO composites using the SPS technique, emphasising the significant influence of graphene content on nanomechanical properties, scratch resistance and electrical conductivity. These findings have implications for the development of advanced materials suitable for various engineering applications requiring robust mechanical properties, scratch resistance and machinability.

2. Materials and methods

2.1. Starting materials

Two raw materials were used. (1) A blend of alumina (Al_2O_3) powder and 17 vol% of silicon carbide whiskers (SiC_w) with commercial name Ceramtuff grade HA9S (Advanced Composite Materials, LLC (Greer, SC, USA), and (2) graphene oxide (GO) prepared from a commercial synthetic graphite powder from Sigma Aldrich (<20 μm, 1.9 % ash content and 99.5 % carbon content) following a modified Hummers' method as described in Ref. [24]. The GO starting material was sonicated for 16 h and was presented as an aqueous suspension with a concentration of 10.6 g/L.

2.2. Processing and sintering

Three composites Al_2O_3-SiC_w-rGO containing 0.5, 1.0 and 1.5 vol% of graphene were prepared. Composition is expressed in wt.% in order to ensure accurate calculation of graphene oxide addition. The experimental procedure for processing the composites is described in detail in Ref. [8]. Briefly, Ceramtuff powders were dispersed in water at pH 10, and were fixed by adding NH_4OH. The slurry was dispersed by stirring for 30 min. Then the aqueous suspension of graphene oxide was added dropwise to the ceramic powder slurry. Magnetic stirring was maintained for 1 h to favour homogeneous mixing. Finally, the slurry was heated under magnetic stirring at 90 °C to reduce the water content and it was then put in an oven at 120 °C overnight to complete the drying process. The dry powders were sieved below 63 μm.

The resulting powders were loaded into a 20 mm graphite die and sintered under vacuum by spark plasma sintering (HP D 25/1, FCT Systeme GmbH, Rauenstein, Germany) up to 1760 °C at a heating rate of 100 °C·min^{-1}, 40 MPa of uniaxial pressure and with a holding time of 5 min at maximum temperature. Samples were identified as Al_2O_3-SiC_w or Al_2O_3-SiC_w-XrGO where X represents the content (vol%) of rGO in the composite.

2.3. Characterisation

GO starting material properties were controlled by a complete characterisation of their composition and physicochemical properties. The carbon, hydrogen and nitrogen contents of the samples were determined by elemental analysis on a LECOCHNS-932 microanalyser. The oxygen content was obtained directly using a LECO-VTF-900 furnace coupled to the microanalyser. The high resolution XPS C1s and O1s spectra were obtained on a VG-Microtech Mutilab 3000 device. The curve fitting of the C1s spectra was performed by applying a Gaussian–Lorentzian peak shape technique and carrying out a Shirley background correction. Infrared spectra were recorded at room temperature using an attenuated total reflection (ATR) mode coupled to a Fourier transform infrared spectrometer (Nicolet 8700FTIR, Thermo Scientific) fitted with a DTS (deuterated triglycine sulfate) detector. The stability of oxygen was monitored by thermogravimetric analysis (TGA) which was carried out using a TA SDT 2960 analyser under a nitrogen flow of 100 mL min^{-1}. Atomic force microscopy (AFM) images were recorded using an atomic force microscope (Cervantes, Nanotec ElectronicaTM) operating under ambient conditions. Microcantilevers with nominal spring constants of k = 40 N/m and a resonance frequency off = 300 kHz were used and WSxM software was employed to control the atomic force microscope and for the data processing of the acquired images.

The microstructural characterisation of fracture surfaces was performed by scanning electron microscopy (FEI Quanta 650 FEG ESEM and Ametek-EDAX coupled EDX analyser, Apollo X detector), as was the observation of the surfaces of samples subjected to wear tests.

Raman spectra were recorded using a Confocal Raman Microscope (WITec, Ulm, Germany) with a 532 nm excitation laser. Up to 10 spectra were recorded along the whole thickness of the polished composites. The sintered samples were previously cut longitudinally in half cylinders with a diamond saw and polished (Struers, model RotoPol-31). The accumulation time for each Raman spectrum was approximately 10 s.

The density of the composites was measured by Archimedes' principle by immersing the sample into liquid water (ASTM C373-88) [25]. Mechanical properties were assessed on surfaces polished down to 1 μm using diamond paste. Hardness and Young's modulus were evaluated employing the nanoindentation technique. The system utilised in this work consists of a nanoindenter (G-200; Agilent Technologies, Barcelona, Spain) with a Berkovich tip previously calibrated with silica standard. Tests were performed under maximum depth control of 1200 nm. The contact stiffness was determined by Continuous Stiffness Measurement technique to calculate the profiles of hardness and elastic modulus. Each sample was tested with a matrix of 25 indentations, whose amplitude were set to 2 nm at a frequency of 45 Hz.

Fracture toughness (K_{IC}) values were studied by the cracks induced by applying loads of 49.0 N for 10 s and an image analysis program and calculated by using the formula proposed by Evans et al. [26]. Six measurements were taken in each sample.

The biaxial flexural strength (σ_f) was measured using the equations of Kirstein and Woolley [27], Vitman and Pukh [28], and the standard specification ASTM F394-78. All tests were obtained at room temperature using a universal testing machine with 50 kN (Instron 856, MA, USA) with a cross-head displacement speed of 0.002 mm s^{-1}.

The scratch resistance of the materials was evaluated using Revetest scratching equipment equipped with a conical geometry diamond indenter (Rockwell) with a 200 μm radius spherical tip. Scratches of 1 cm in length were made, progressively increasing the load applied along them, from 0 to 180 N. Before and after scratching the surface, the indenter ran along the area to be tested applying a minimum load, thereby recording the original profile of the surface; this way it was possible to detect the changes in depth on the scratched area. The friction force was also recorded during the execution of the scratch. To avoid errors caused by the possible presence of specific defects on the tested surface, which could have influenced the test, three scratches were always made on each surface. In order to visually observe the changes in the scratching mechanism, micrographs of the scratches were obtained using an optical microscope.

The electrical resistivity variation of the samples as a function of GO content was measured using a two-channel nano-voltmeter (Keithley 2182 A, Cleveland, OH, USA) with silver paste contacts and a separate current source (Keithley 6220, Cleveland, OH, USA).

Cutting tool inserts were machined from SPS samples with standard SNGN geometry (square, 0° relief angle, ±0.025 mm nose height/inscribed circle and ±0.13 mm thickness tolerances, no hole). The rear surface wear, which occurs during $100Cr_6$ cylindrical steel sample machining, was taken as a criterion of quality of the cutting insert. Longitudinal turning of steel specimens was performed under the following conditions: cutting speed V = 300 m/min, traverse speed S = 0.05 mm/rev and depth of cut t = 0.5 mm. The rear wear limit was taken to be h = 0.4 mm. For comparison purposes, commercial inserts from SANDVIK Coromant, reference: CC670, were also used.

3. Results and discussion

3.1. Graphene oxide properties

The combination of the oxidation step with the liquid phase exfoliation treatment for long periods of time, in this case 16h in a sonication bath, contributed to a high content of oxygenated functional groups, since small lateral size layers were obtained containing a large amount of oxygenated functional groups mainly located at the edges of the GO layers. The oxygen content in the GO went up to 43.0 wt% with O/C ratio of 1.7. The sample also presented a low content of nitrogen (0.2 wt %), sulfur (1.5 wt%) and a 3.0 wt% of hydrogen mainly from the oxidation methodology.

Through the characteristic Fourier-transform infrared spectroscopy (FTIR) of GO, depicted in Fig. 1a, it can be seen that the oxygen content is due to the contribution of several oxygen functional groups. The spectrum showed a prominent O–H stretching band between 3750 cm^{-1} and 2500 cm^{-1}, primarily arising from carboxyls and hydroxyls with a

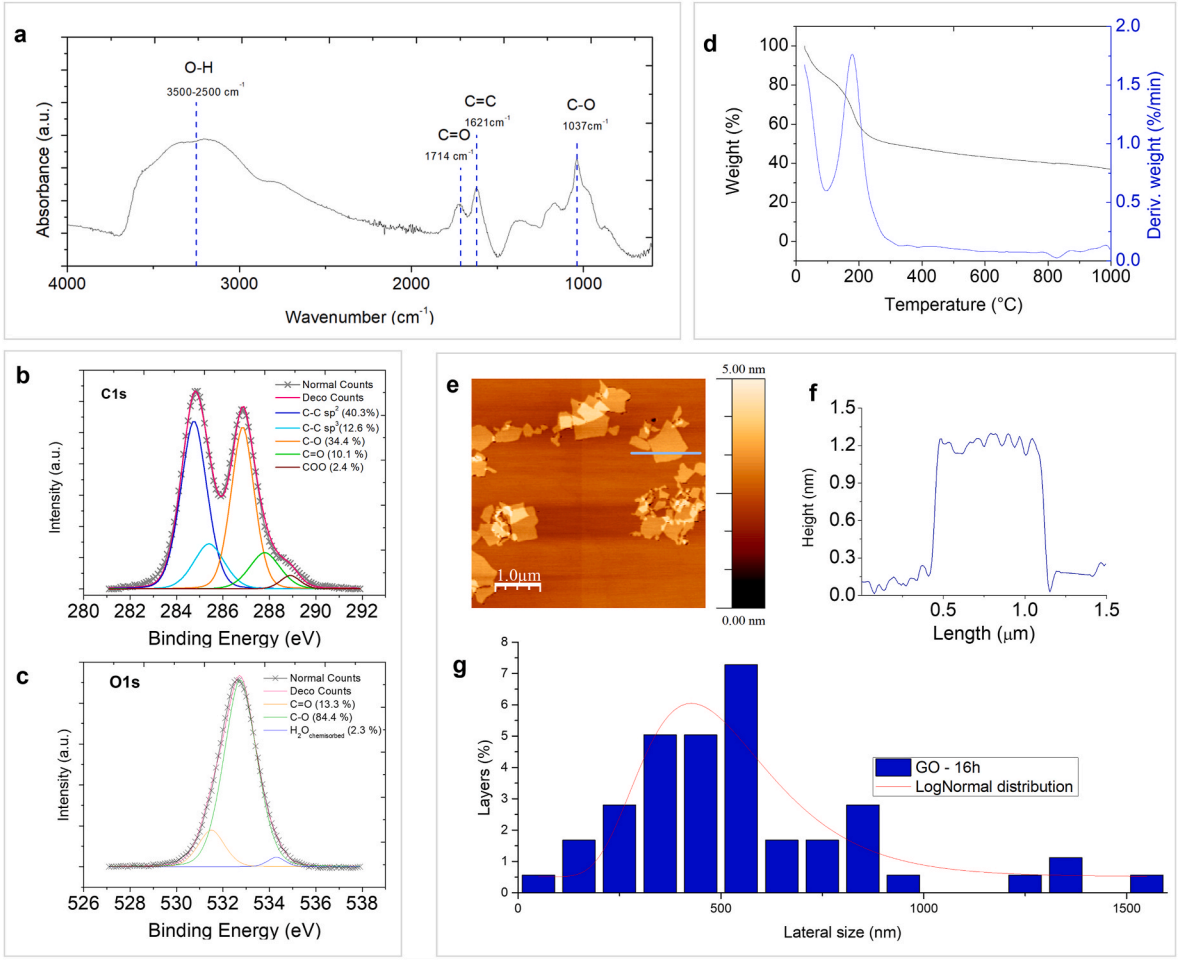

Fig. 1. (a) FTIR spectrum of GO with its characteristics bands. (b) Deconvoluted high resolution XPS spectra of C1s and (c) O1s. (d) TGA and DTG of the GO with a rate of 5 °C/min up to 1000 °C under N_2 atmosphere. (e) AFM image of GO with (f) the height profile corresponding to the blue line and (g) the distribution of the lateral size of the GO layers. (For interpretation of the references to colour in this figure legend, the reader is referred to the Web version of this article.)

contribution from physiosorbed H_2O. The stretching vibration of carbonyl (C═O) with a band at 1714 cm^{-1} contributed to the carboxylic groups. In addition, the aromatic vibration (C═C) from unoxidised graphitic domains can be observed, which exhibited its characteristic band at 1620 cm^{-1}. The C–O showed the absorbance band at 1037 cm^{-1} [29]. However, FTIR spectra are not sufficient to clearly distinguish carboxylic from carbonyl groups. According to Gao et al. (31) the epoxy and hydroxy groups are located all over the layers while carbonyl groups are only located at the edges of the layers.

The high resolution C1s and O1s XPS spectra made it possible to identify and quantify the oxygen functional groups content. The C1s spectrum (Fig. 1b) exhibited a well-defined double peak formation, which is a signature of the oxidation in GO. The aromatic lattice only represented a content of 40.3 wt%. There was a contribution of the C–O (286.6 eV) and C═O (287.5 eV) observed in FTIR spectrum. The highest contribution of oxygen functional groups was due to the C–O (34.4 wt%) with a low contribution of C═O (10.1 wt%) and COO (2.4 wt%). This behaviour was also confirmed by the deconvolution of the O1s high resolution spectrum (Fig. 1c), with an 84.4 wt% in C–O content and a 2.3 wt% of oxygen related to chemisorbed water.

The TGA/derivative thermogravimetry (DTG) was performed on the sample to confirm the stability of the oxygen functional groups (Fig. 1d). The GO started to lose mass upon heating even below 100 °C, which is associated with elimination of loosely bound or adsorbed water and gas molecules. The major mass loss can be observed along with an exothermic signal of mass loss rate (dW/dT) around 200 °C, yielding CO, CO_2 and steam as a byproduct of the reduction process, due to the presence of more unstable oxygen functional groups: carboxyl and hydroxyl groups. According to the mechanisms proposed by Gao et al. [30] the oxygen functionalities attached to the interior of an aromatic domain are removed more easily than those attached to the edges of the aromatic domain.

The GO layers were studied through AFM (Fig. 1e). Firstly, the blue line on the surface of the GO layer corresponds to the profile height (Fig. 1f) which presented a height of 1.1 ± 0.1 nm, typical of GO. Secondly, from the histogram (Fig. 1g), it can be observed that the large ultrasonic treatment leads to a low lateral size of GO layers, and it can be concluded that the 91 % of the sample presents a lateral size lower than 1 μm. The data was adjusted to a log-normal function and the average diameter was 520 ± 50 nm.

3.2. Raman characterisation of sintered composites

The determination of graphene presence in sintered composites at 1760 °C by SPS was performed using Raman spectroscopy. In Fig. 2, the intensity peaks are visible, showing information about the sample composition [20]. The first peak at 800 cm^{-1} is the most intense and is present in all samples, as it corresponds to the presence of SiC whiskers. A second peak around 1400 cm^{-1}, labelled as "D" indicates the existence of out-of-plane vibration modes of graphene. This peak only occurs in samples where the carbon lattice is distorted due to some defect. A second-order spectrum can be found at 2700 cm^{-1} and it is very sensitive to the number of layers of graphene [31]. It is one of the indicators of graphene presence in the sample. A third peak near 1600 cm^{-1}, labelled as "G" indicates the existence of in-plane vibration modes in any sp^2-hybridised carbon compound, such as graphene [24]: The intensity of these peaks is directly dependent on the graphene content in the samples. In samples with a higher proportion of rGO, these peaks are more pronounced than in samples with a lower content of graphene.

3.3. Mechanical properties

All the composites were fully densified by Spark Plasma Sintering process (the relative density was calculated using the rule of mixtures) with relative density higher than 99 % (Table 1). It is important to note that the complete densification of Al_2O_3-SiC_w requires a higher sintering

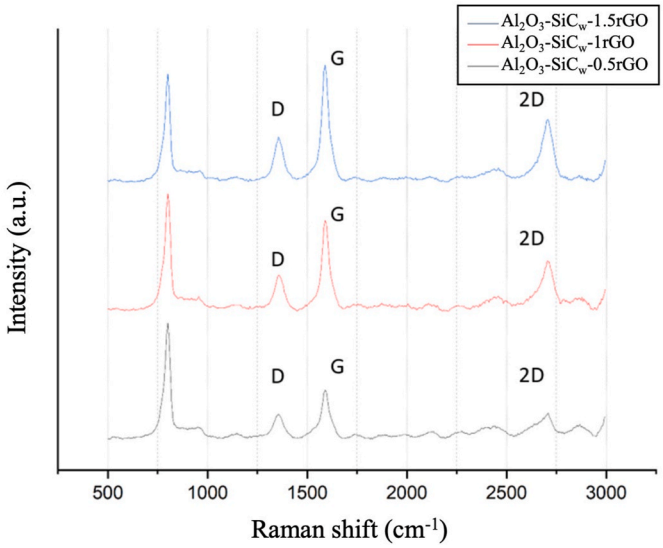

Fig. 2. Raman characterization of sintered composites by SPS at 1760 °C-5 min.

temperature. In this sense, previous works have shown that a sintering temperature over 1750 °C is needed [8] to achieve complete densification of Al_2O_3-SiC_w materials with similar composition ratios to those studied in this work. For this reason, 1760 °C was selected as sintering temperature for all the compositions. Table 1 shows the density, alumina grain size and mechanical properties of composite materials sintered at 1760 °C-5 min.

According to the results the density and mechanical properties increase with a low content of rGO (0.5%vol.) and then these values decrease as the amount of rGO increases (1 and 1.5%vol. rGO). This behaviour in mechanical properties can be attributed, on the one hand, to the fact that low graphene contents very effectively inhibit grain growth in the matrix, thus minimizing graphene aggregation. However, not all graphene percentages have a positive effect on the mechanical properties. It has been observed that graphene contents >1%vol. GO slightly lower the mechanical properties. This may be due to the difficulty of sintering materials with carbonaceous second phases. Furthermore, it can be observed that small amounts of graphene increase the flexural strength, reaching values close to 920 MPa with only 0.5 vol%. The high fracture toughness values obtained in composites reinforced with graphene can also be observed. Graphene seems to be an optimal reinforcement for Al_2O_3-SiC_w composites, as referred to by Grigoriev et al. [8], since it improves the operational reinforcement mechanisms, maintains the stiffness of the material and, as a consequence, improves both toughness and fracture toughness.

Fig. 3 shows the hardness and Young's modulus curves and their evolution with indenter penetration depth. The hardness values obtained in all cases are exceptional and remain constant with the depth of indentation. The average values in the indentation range from 200 to 800 nm as shown in Table 1. The scatter of H_V and E is very large for the initial 200 nm penetration depth. This could be due to the implied experimental variability of factors such as tip-sample interactions, sample roughness and tip rounding. In all cases, values exceeding 28 GPa were achieved. The values of hardness obtained by He et al. [32], using hot oscillatory pressing (HOP), dynamic sinter forging (DSF) and oscillatory pressure-assisted sinter forging (OPSF) at 1700 °C were 15.3, 22.5 and 23.7 GPa, respectively. Zhu et al. [33] achieved 21.3 GPa of hardness for Al_2O_3-25 vol% SiC_w obtained at 1750 °C by OPS. In this research, we have improved these values by more than 20 %. Therefore, a slight decrease in hardness can be observed with increasing GO content, with a difference of only 5 %. This reduction aligns with the trend observed in the obtained densification levels and other authors [8,9]. As

Table 1
Relative density, alumina grain size and mechanical properties of sintered composites by SPS at 1760 °C-5 min.

Sample	Relative density (%)	Al_2O_3 grain size (μm)	Flexural strength (MPa)	Fracture toughness (MPa·$m^{1/2}$)	Hardness[a] (GPa)	Young's moludus[a] (GPa)
Al_2O_3-SiC_w	99.0 ± 0.1	1.8 ± 0.5	750 ± 39	9.52 ± 0.27	28.8 ± 0.7	431.2 ± 5.8
Al_2O_3-SiC_w-0.5rGO	99.5 ± 0.1	1.3 ± 0.3	919 ± 45	10.55 ± 0.31	29.9 ± 0.9	441.8 ± 6.9
Al_2O_3-SiC_w-1rGO	99.5 ± 0.1	1.2 ± 0.3	843 ± 49	9.61 ± 0.87	28.6 ± 1.3	434.4 ± 9.8
Al_2O_3-SiC_w-1.5rGO	99.2 ± 0.1	1.1 ± 0.2	802 ± 43	9.15 ± 0.47	28.3 ± 1.1	418.9 ± 7.0

[a] The average values in the indentation range of 200–800 nm.

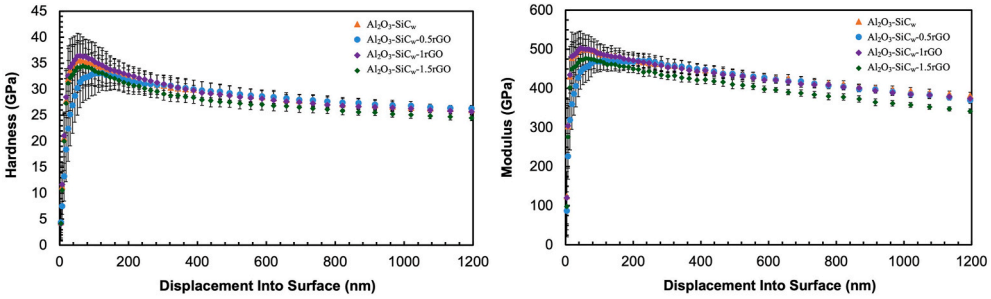

Fig. 3. Evolution of the mechanical properties (Hardness and Young modulus) as a function of graphene content with penetration depth.

for the elastic modulus, the values obtained reflect a moderate influence of graphene content and show a slight decrease as a function of penetration depth. This may be due to residual stresses in the material obtained by the SPS process [34]. The rapid heating of the SPS technique introduces stresses that can lead to the formation of microcracks under the indentation tip.

3.4. Microstructural characterization

Fig. 4 shows the representative fracture surface of the sintered samples. As for the grain size of Al_2O_3 particles, the addition of a second rGO phase clearly affects the decrease of the matrix grain size during sintering, compared to the pure Al_2O_3-SiC_w sample, where large and uneven alumina grains are observed (Table 1). Consequently, the average grain size of the Al_2O_3 matrix grains decreases with increasing rGO content. This reduction in grain size can be attributed to the distribution of rGO between the ceramic grain boundaries, resulting in a refinement of the microstructure. However, the more important microstructural feature is the change in the Al_2O_3-SiC_w of the interfacial energy. The composites without graphene showed how the Al_2O_3 grains grew during sintering around the SiC_w crystals, in many cases occupying an intragranular position. In the case of composites with rGO it can be observed how very small amounts of rGO drastically modify the Al_2O_3-SiC_w interfacial energy by reducing the number of SiC_w in intragranular

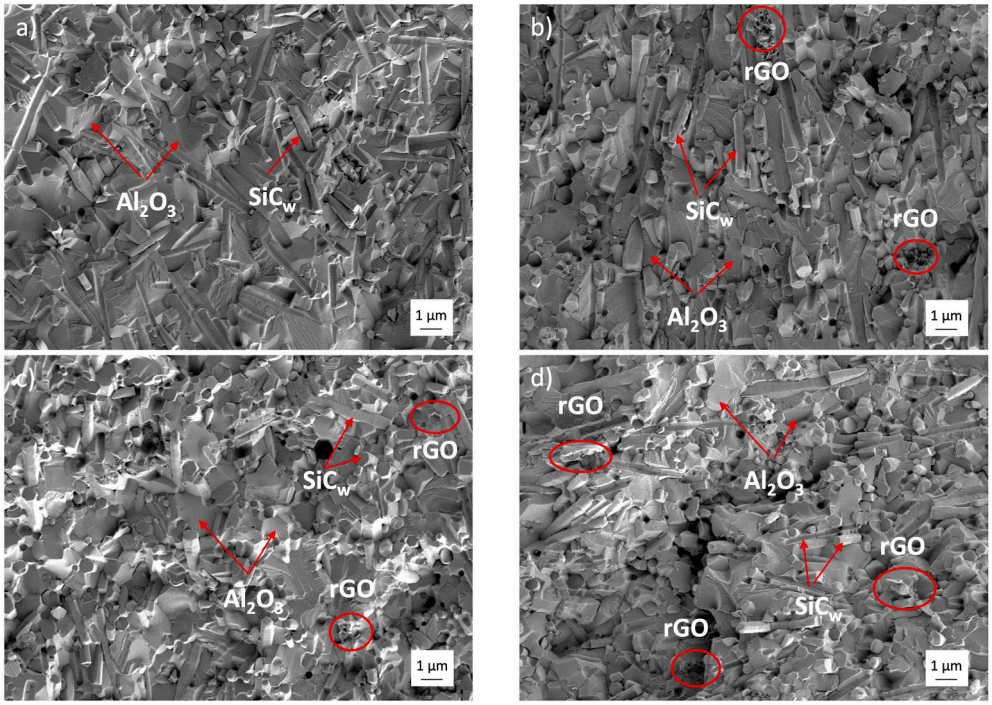

Fig. 4. Fracture surface micrographs: a) Al_2O_3-SiC_w, b) Al_2O_3-SiC_w-0.5rGO, c) Al_2O_3-SiC_w-1rGO, d) Al_2O_3-SiC_w-1.5rGO.

positions. In addition, only in the case of the 0.5rGO and 1rGO composites were some whiskers kept in intragranular positions and in the 1.5rGO composite only intergranular positions were observed with a clear reduction of the alumina grain size.

Fig. 5 shows a FESEM image of the fracture surface of the sintered 1rGO composite. This image confirms that the graphene is well distributed in the ceramic matrix. The interfaces play a significant role in Al_2O_3-SiC_w composites, and the graphene presence can enhance the already remarkable reinforcement provided by the whiskers due to pullout processes or extrinsic strengthening mechanisms that occur in the wake region.

3.5. Scratch resistance

After performing the test, we can determine the critical scratch loads, the depth of the footprint generated and the total deformation experienced by the materials, finally evaluating the scratch resistance. Fig. 6a shows the total depth reached in the studied surfaces of each of the samples, calculated as the difference between the profile during loading and the original profile of the sample. Fig. 6b shows, after scratching, the depth reached by the indenter. The plastic deformation of the surface studied, calculated as the difference between the profile obtained after the test and the original profile of the sample is shown.

Table 2 presents the mean values of critical loads determined from scratch tests. The concept of critical load implies a value of applied load for which a change of mechanism occurs during scratching. In this case, two different critical loads have been defined on the tested specimen: the critical load value Lc_1, which corresponds to the load at which longitudinal cracks start to form, while the critical load value Lc_2 corresponds to the beginning of spalling.

Figs. 7 and 8 shows the images obtained by optical microscopy of the scratch grooves for the tested sample, in which the different critical loads observed have been identified. It should be noted that the images show an example of a specific scratch test, while the critical load values are average values of the three tests performed.

From the results obtained, it can be concluded that the higher the graphene content, the greater the depth reached during the test. This fact indicates a direct relationship between the graphene content and the hardness of the material: samples with a higher proportion of graphene have lower hardness. The increase in graphene content has no influence on the initiation of cracks, as is reflected in the small variation of the critical load values Lc1. On the other hand, there is an increase in the value of the critical load Lc2, i.e., the load required to initiate the spalling of the material, so that despite the possible decrease in hardness, the pull-out resistance of the material is improved, a characteristic recommended for its application as a cutting tool. It should also be noted that the samples with higher graphene content showed greater plastic deformation, and greater total deformation during the test. This fact suggests a possible reduction of the rigid and brittle nature of the composite.

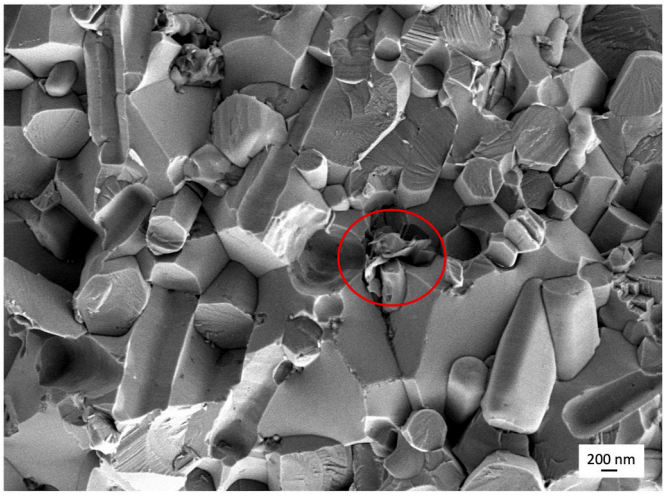

Fig. 5. Micrograph of a fracture surface of an Al_2O_3-SiC_w-1rGO composite, in which the rGO layers can be easily identified (circle).

3.6. Electrical properties

The electrical resistivity of the sintered composites decreases with increasing graphene content, as shown in Fig. 9a. According to the literature an electroconductive material is obtained through the addition of 1 vol% of rGO. This characteristic is important from a processing point of view, considering that SPS heating consists of passing a continuous pulsed electric current through the graphite mould and the sample, if conductive rGO acts as a sintering additive. Therefore, graphene sheets allow the electrical current to pass homogeneously through the sample, enhancing effective heating and thereby reducing the maximum temperature required for complete densification and strengthening the interfaces between the components. The EDM technique is used for efficient machining when the materials show an electrical resistivity below 100–300 Ω cm. In our case a composition of graphene as low as 0.5 wt% could be appropriate for EDM machining.

Considering these promising results and starting from the fact that many commercial cutting tools are based on Al_2O_3-SiC_w composites, this study explored the possibility of fabricating cutting tools from the Al_2O_3-SiC_w-1rGO sample and comparing them with Sandvik inserts, based on Al_2O_3-SiC_w. Both types of cutting tools were compared by turning $100Cr_6$ steel (quality F.1310) cylindrical samples, following the conditions described in the experimental part. Fig. 9b shows the length of the segment machined until reaching the limit of 0.4 mm wear on the backside of the cutting edge. The evolution of surface Ra and Rz are also represented as a measurement of machined surface quality. The segment machined with the rGO-functionalised cutting tool was 7.7 times longer than the segment machined with the commercial insert, confirming the data obtained during wear behaviour comparison. Moreover, the surface roughness of the machined cylinder was lower when rGO-functionalised cutting tools were used throughout the entire test, especially at the beginning. It has been demonstrated that the addition of rGO to Al_2O_3-SiC_w composites leads to an increase in mechanical properties such as hardness and fracture toughness, which is attributed to the strengthening of grain interfaces. This mechanical improvement is responsible for their enhanced wear resistance, which finally leads to a better performance under real conditions, in comparison with Al_2O_3-SiC_w commercial inserts.

4. Conclusions

The fabrication of graphene oxide (GO) and Al_2O_3-SiC_w composites through spark plasma sintering has demonstrated mechanical improvements, particularly when small volumes of graphene are uniformly dispersed in the matrix. This dispersion of graphene at the boundaries of Al_2O_3-SiC_w enhances various extrinsic reinforcement mechanisms, such as material removal observed during scratch tests. Among the fabricated composites, the one containing 0.5 vol% GO exhibited the highest mechanical properties, including flexural strength (919 ± 45 MPa), fracture toughness (10.6 ± 0.3 MPa $m^{1/2}$), and hardness (30 ± 0.9 GPa). Notably, compared to Al_2O_3-SiC_w composites without GO, this composite demonstrated a significant increase in flexural strength of approximately 20 %. Moreover, this composite with 0.5 vol% GO showed an electrical resistivity ranging from 300 to 100 Ω cm, indicating its suitability for applications such as electrical discharge machining. Finally, two types of cutting tools were tested under real conditions, commercial Al_2O_3-SiC_w inserts and inserts manufactured with the material studied in this work. The incorporation of 1 vol% GO enabled machining segments seven times longer than with commercial

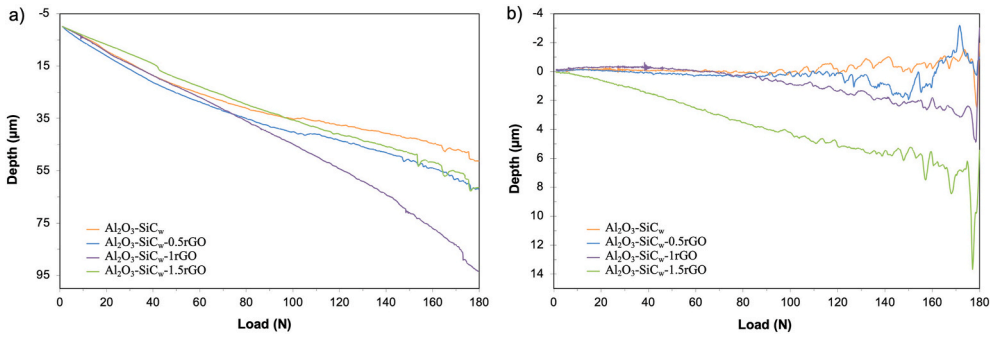

Fig. 6. a) Total deformation of the samples during the test and, b) Depth by plastic deformation mechanisms experimented by the samples tested.

Table 2
Average critical load values Lc (N).

Composite	Lc_1 (N)	Lc_2 (N)
Al_2O_3-SiC_w	73 ± 2	108 ± 4
Al_2O_3-SiC_w-0.5rGO	72 ± 3	116 ± 5
Al_2O_3-SiC_w-1rGO	72 ± 1	137 ± 2
Al_2O_3-SiC_w-1.5rGO	72 ± 2	138 ± 2

inserts.

In summary, the incorporation of graphene oxide into Al_2O_3-SiC_w composites enhances their mechanical properties and electrical conductivity, making them promising materials for various engineering applications, including those requiring high strength and electrical conductivity. Further studies are crucial for investigating and theoretically modelling the different types of graphene/ceramic interfaces that have been experimentally developed and their impact on the reinforcing mechanism within the composite. Understanding these interfaces in depth will facilitate the processing and design of composites with the most advantageous properties.

CRediT authorship contribution statement

Marta Suárez: Writing – review & editing, Writing – original draft, Methodology, Investigation, Conceptualization. **Rut Benavente:** Writing – review & editing, Writing – original draft, Methodology, Investigation, Conceptualization. **Amparo Borrell:** Writing – review & editing, Writing – original draft, Methodology, Investigation, Conceptualization. **Ana M. Pérez-Mas:** Writing – review & editing, Methodology, Investigation. **Rosa Menéndez:** Writing – review & editing, Supervision, Conceptualization. **Carlos F. Gutiérrez:** Writing – review & editing, Methodology, Investigation. **Adolfo Fernández:** Writing – review & editing, Supervision, Conceptualization.

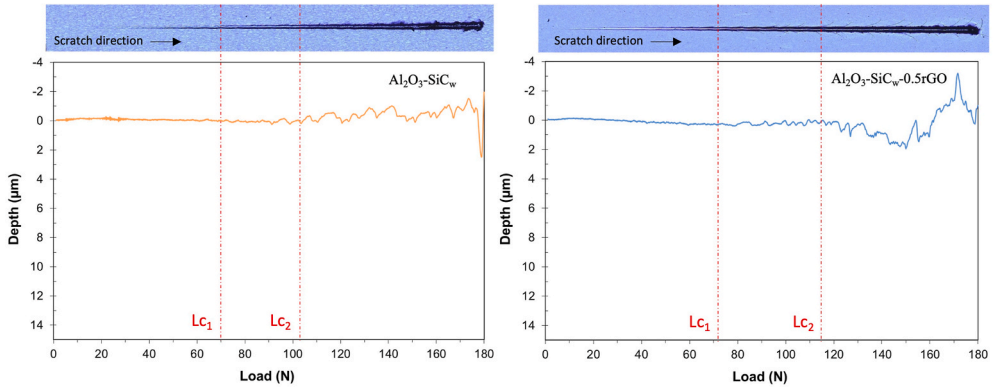

Fig. 7. Microscopy image of the scratch test and graph of depth reached by plastic deformation of the sample Al_2O_3-SiC_w and Al_2O_3-SiC_w-0.5rGO.

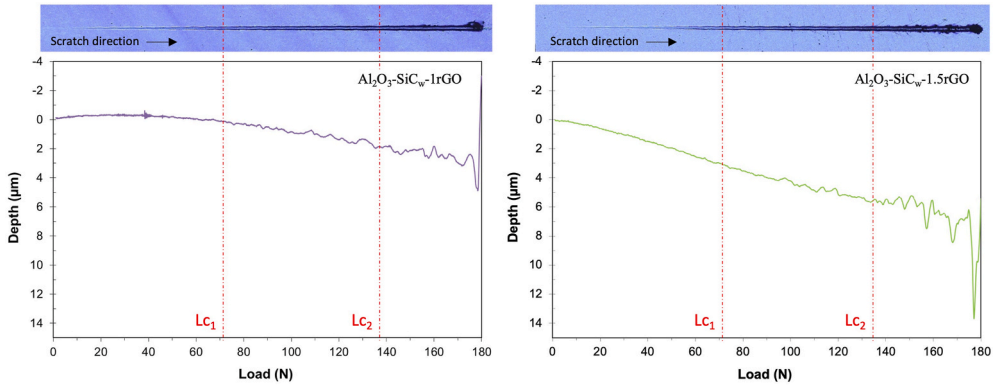

Fig. 8. Microscopy image of the scratch test and graph of depth reached by plastic deformation of the sample Al_2O_3-SiC_w-1rGO and Al_2O_3-SiC_w-1.5rGO.

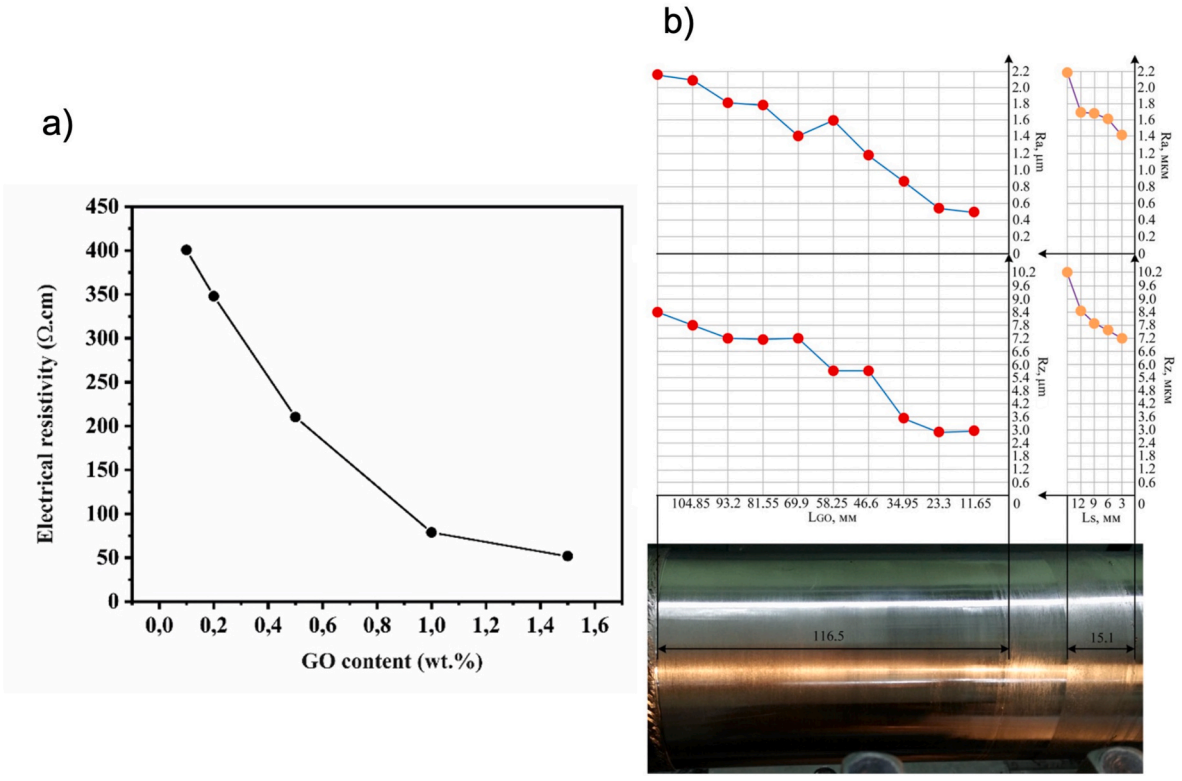

Fig. 9. a) Electrical resistivity of the sintered composites depends on the graphene content. b) Comparison of the cutting tools' lifetime, with and without rGO addition, and of the surface quality of the machined steel.

Declaration of competing interest

The authors declare that they have no known competing financial interests or personal relationships that could have appeared to influence the work reported in this paper.

Acknowledgements

This publication is part of the grant PID2021-128548OB-C21&C22 funded by MCIN/AEI/10.13039/501100011033. CINN–CSIC acknowledges the project CPP2022-009892. Authors are grateful to Moscow State University of Technology "Stankin" for the evaluation of the material under real conditions.

References

[1] Cutting tool materials, in: W. Grzesik (Ed.), Advanced Machining Processes of Metallic Materials, Elsevier, 2008, pp. 35–63, 978-0-08-044534-2.
[2] B. Liu, W. Wei, Y. Gan, Ch Duan, H. Cui, Preparation, mechanical properties and microstructure of TiB2 based ceramic cutting tool material toughened by TiC whisker, Int. J. Refract. Hard. Met. 93 (2020) 105372, https://doi.org/10.1016/j.ijrmhm.2020.105372.
[3] P. Campos, J.P. Davim, J.R. Ferreira, A.P. Paiva, P.P. Balestrassi, The Machinability of Hard Materials – A Review in: Machinability of Advanced Materials, John Wiley & Sons, Inc, 2014, pp. 145–173, https://doi.org/10.1002/9781118576854.ch5.
[4] W. Liu, H. Wu, Y. Xu, L. Lin, Y. Li, S. Wu, Cutting performance and wear mechanism of zirconia toughened alumina ceramic cutting tools formed by vat photopolymerization-based 3D printing, Ceram. Int. 49 (2023) 23238–23247, https://doi.org/10.1016/j.ceramint.2023.04.153.
[5] J. Zhanga, G. Xiao, M. Yi, Z. Chen, J. Zhang, H. Chen, X. Shang, Ch Xu, Mechanical properties of ZrB2/SiC/WC ceramic tool materials from room temperature to 1100 °C and cutting performance, Int. J. Refract. Hard. Met. 101 (2021) 105697, https://doi.org/10.1016/j.ijrmhm.2021.105697.
[6] A. Borrell, I. Álvarez, R. Torrecillas, V.G. Rocha, A. Fernández, Microstructural design for mechanical and electrical properties of spark plasma sintered Al2O3–SiC nanocomposites, Mater. Sci. Eng. 534 (2012) 693–698, https://doi.org/10.1016/j.msea.2011.12.032.
[7] K. Bonny, P. De Baets, J. Vleugels, A. Salehi, O. Van der Biest, B. Lauwers, W. Liu, Influence of electrical discharge machining on tribological behavior of ZrO2-TiN composites, Wear 265 (2008) 1884–1892, https://doi.org/10.1016/j.wear.2008.04.033.
[8] S. Grigoriev, P. Peretyagin, A. Smirnov, W. Solís, L.A. Díaz, A. Fernández, R. Torrecillas, Effect of graphene addition on the mechanical and electrical properties of Al2O3-SiCw ceramics, J. Eur. Ceram. Soc. 37 (2017) 2473–2479, https://doi.org/10.1016/j.jeurceramsoc.2017.01.027.
[9] C.F. Gutiérrez-González, M. Suárez, S. Pozhidaev, S. Rivera, P. Peretyagin, W. Solís, L.A. Díaz, A. Fernández, R. Torrecillas, Effect of TiC addition on the mechanical behaviour of Al2O3-SiC whiskers composites obtained by SPS, J. Eur. Ceram. Soc. 36 (2016) 2149–2152, https://doi.org/10.1016/j.jeurceramsoc.2016.01.050.
[10] A.K. Geim, Graphene: status and prospects, Science 324 (2009) 1530–1534, https://doi.org/10.1126/science.1158877.
[11] K.S. Novoselov, V.I. Fal'Ko, L. Colombo, P.R. Gellert, M.G. Schwab, K. Kim, A roadmap for graphene, Nature 490 (2012) 192–200, https://doi.org/10.1038/nature11458.
[12] Y. Zhang, T. Bai, Influence of graphene orientation on tribological properties of organic composite coatings from the perspective of energy transfer using molecular dynamics, Tribol. Int. 193 (2024) 109368, https://doi.org/10.1016/j.triboint.2024.109368.
[13] H. Kim, A.A. Abdala, C.W. MacOsko, Graphene/polymer nanocomposites, Macromolecules 43 (2010) 6515–6530, https://doi.org/10.1021/ma100572e.
[14] J.R. Potts, D.R. Dreyer, C.W. Bielawski, R.S. Ruoff, Graphene-based polymer nanocomposites, Polymer 52 (2011) 5–25, https://doi.org/10.1016/j.polymer.2010.11.042.
[15] K. Markandan, J.K. Chin, M.T.T. Tan, Recent progress in graphene based ceramic composites: a review, J. Mater. Res. 32 (2017) 84–106, https://doi.org/10.1557/jmr.2016.390.
[16] A. Nieto, A. Bisht, D. Lahiri, C. Zhang, A. Agarwal, Graphene reinforced metal and ceramic matrix composites: a review, Int. Mater. Rev. 62 (2017) 241–302, https://doi.org/10.1080/09506608.2016.1219481.
[17] C. Ramirez, M.I. Osendi, P. Miranzo, M. Belmonte, F. Figueiredo, A. Castro-Beltrán, M. Terrones, Graphene nanoribbon ceramic composites, Carbon 90 (2015) 207–214, https://doi.org/10.1016/j.carbon.2015.04.014.
[18] N.W. Solís, P. Peretyagin, R. Torrecillas, A. Fernández, J.L. Menéndez, C. Mallada, L.A. Díaz, J.S. Moya, Electrically conductor black zirconia ceramic by SPS using graphene oxide, J. Electroceram. 38 (2017) 119–124, https://doi.org/10.1007/s10832-017-0076-z.
[19] R. Sedlák, A. Kovalčíková, V. Girman, E. Múdra, P. Rutkowski, A. Dubiel, J. Dusza, Fracture characteristics of SiC/graphene platelet composites, J. Eur. Ceram. Soc. 37 (2017) 4307–4314, https://doi.org/10.1016/j.jeurceramsoc.2017.04.067.
[20] R. Sedlák, A. Kovalčíková, E. Múdra, P. Rutkowski, A. Dubiel, V. Girman, R. Bystrický, J. Dusza, Boron carbide/graphene platelet ceramics with improved fracture toughness and electrical conductivity, J. Eur. Ceram. Soc. 37 (2017) 3773–3780, https://doi.org/10.1016/j.jeurceramsoc.2017.04.061.

[21] A. Centeno, V.G. Rocha, B. Alonso, A. Fernández, C.F. Gutierrez-Gonzalez, R. Torrecillas, A. Zurutuza, Graphene for tough and electroconductive alumina ceramics, J. Eur. Ceram. Soc. 33 (2013) 3201–3210, https://doi.org/10.1016/j.jeurceramsoc.2013.07.007.
[22] A. Borrell, V.G. Rocha, R. Torrecillas, A. Fernández, Effect of carbon nanofibers content on thermal properties of ceramic nanocomposites, J. Compos. Mater. 46 (2013) 1229–1234, https://doi.org/10.1177/0021998311416528.
[23] A. Borrell, O. García-Moreno, R. Torrecillas, V. García-Rocha, A. Fernández, Lithium aluminosilicate reinforced with carbon nanofiber and alumina for controlled-thermal-expansion materials, Sci. Technol. Adv. Mater. 13 (2012) 015007, https://doi.org/10.1088/1468-6996/13/1/015007.
[24] C. Botas, A.M. Pérez-Mas, P. Álvarez, R. Santamaría, M. Granda, C. Blanco, R. Menéndez, Optimization of the size and yield of graphene oxide sheets in the exfoliation step, Carbon (2013) 576–578, https://doi.org/10.1016/j.carbon.2013.06.096.
[25] ASTM C373-14. Standard Test Method for Water Absorption, Bulk Density, Apparent Porosity, and Apparent Specific Gravity of Fired Whiteware Products.
[26] A.G. Evans, E.A. Charles, Fracture toughness determinations by indentation, J. Am. Ceram. Soc. 59 (1976) 371–372, https://doi.org/10.1111/j.1151-2916.1976.tb10991.x.
[27] A.F. Kirstein, R.M. Woolley, Symmetrical bending of thin circular elastic plates on equally spaced point supports, J. Res. Natl. Bur. Stand. C 71 (1967) 1–10, https://doi.org/10.6028/JRES.
[28] F.F. Vitman, V.P. Pukh, A method for determining the strength of sheet glass, Zavod. Lab. 29 (1963) 863–867, https://doi.org/10.1007/BF00681213.
[29] C. Gong, S. Kim, S. Zhou, Y. Hu, M. Acik, W. De Heer, C. Berger, A. Bongiorno, E. Riedo, Y. Chabal, Chemical bonding and stability of multilayer graphene oxide layers, in: Proceedings of SPIE – Int. Soc. Opt. Eng., 2014, https://doi.org/10.1117/12.2045554.
[30] X. Gao, J. Jang, S. Nagase, Hydrazine and thermal reduction of graphene oxide: reaction mechanisms, product structures, and reaction design, J. Phys. Chem. C 114 (2010) 832–842, https://doi.org/10.1021/jp909284g.
[31] A.C. Ferrari, J.C. Meyer, V. Scardaci, C. Casiraghi, M. Lazzeri, F. Mauri, S. Piscanec, D. Jiang, K.S. Novoselov, S. Roth, A.K. Geim, Raman spectrum of Graphene and Graphene layers, Phys. Rev. Lett. 97 (2006) 187401, https://doi.org/10.1103/PhysRevLett.97.187401.
[32] H. He, Ch Ma, B. Song, R. Zhao, P. Zhao, H. Wang, D. Han, H. Lu, H. Xu, R. Zhang, L. An, G. Shao, A novel sintering method of Al2O3/SiCw ceramic composites with improved wear resistance: oscillatory pressure-assisted sinter forging, Ceram. Int. 49 (2023) 34223–34231, https://doi.org/10.1016/j.ceramint.2023.08.136.
[33] T. Zhu, W. Guo, J. Zhang, S. Sang, Y. Li, Z. Xie, X. Liang, H. Wang, Y. Han, Synergistic toughening effect of SiC whiskers and particles in ZrO2–Al2O3–SiC ceramics, Ceram. Int. 49 (2023) 36337–36343, https://doi.org/10.1016/j.ceramint.2023.08.317.
[34] I. Alvarez-Clemares, A. Borrell, S. Agouram, R. Torrecillas, A. Fernandez, Microstructure and mechanical effects of spark plasma sintering in alumina monolithic ceramics, Scripta Mater. 68 (2013) 603–606, https://doi.org/10.1016/j.scriptamat.2012.12.016.